Commun. Comput. Phys.
doi: 10.4208/cicp.OA-2016-0112

Vol. **22**, No. 2, pp. 473-493
August 2017

Three-Dimensional Cavitation Bubble Simulations based on Lattice Boltzmann Model Coupled with Carnahan-Starling Equation of State

Yanwen Su, Xuelin Tang*, Fujun Wang, Xiaoqin Li and Xiaoyan Shi

Beijing Engineering Research Centre of Safety and Energy Saving Technology for Water Supply Network System, China Agricultural University, Beijing 100083, China.

Received 19 July 2016; Accepted (in revised version) 6 January 2017

Abstract. The Shan-Chen multiphase lattice Boltzmann model (LBM) coupled with Carnahan-Starling real-gas equation of state (C-S EOS) was proposed to simulate three-dimensional (3D) cavitation bubbles. Firstly, phase separation processes were predicted and the inter-phase large density ratio over 2×10^4 was captured successfully. The liquid-vapor density ratio at lower temperature is larger. Secondly, bubble surface tensions were computed and decreased with temperature increasing. Thirdly, the evolution of creation and condensation of cavitation bubbles were obtained. The effectiveness and reliability of present method were verified by energy barrier theory. The influences of temperature, pressure difference and critical bubble radius on cavitation bubbles were analyzed systematically. Only when the bubble radius is larger than the critical value will the cavitation occur, otherwise, cavitation bubbles will dissipate due to condensation. According to the analyses of radius change against time and the variation ratio of bubble radius, critical radius is larger under lower temperature and smaller pressure difference condition, thus bigger seed bubbles are needed to invoke cavitation. Under higher temperature and larger pressure difference, smaller seed bubbles can invoke cavitation and the expanding velocity of cavitation bubbles are faster. The cavitation bubble evolution including formation, developing and collapse was captured successfully under various pressure conditions.

AMS subject classifications: 65E05, 76B10, 76T10

Key words: Cavitation bubble, Carnahan-Starling equation of state, lattice Boltzmann model, Shan-Chen multiphase model, 3D numerical simulation.

*Corresponding author. *Email addresses:* ysu1452@163.com(Y. Su), xl-tang@mail.tsinghua.edu.cn (X. Tang), wangfj@cau.edu.cn (F. Wang), 13522915056@163.com (X. Li), sxy36@163.com (X. Shi)

 ©2017 Global-Science Press

https://doi.org/10.4208/cicp.OA-2016-0112 Published online by Cambridge University Press

1 Introduction

Cavitation is defined as a rapid formation and collapse of vapor bubbles in a flow due to pressure falling below the liquid's vapor pressure [1]. The very fast and energy-focusing collapse of cavities [2] companied with cavitation always causes the adverse effects of noise, pressure pulsation, vibration and erosion in fluid machinery, propeller in the propulsion device, or the cascades of turbomachinery [3]. The dynamics of cavitation bubble is complex, including high non-linearity, mass transfer [4] and generating of shock waves [5]. Cavitation occurs either as "homogeneous" for the limit of the pure liquid tension, or as "heterogeneous" for nucleation caused by preexisting bubbles in a fluid [6]. The occurrence of cavitation depends on the vapor pressure and the size of the cavitation bubble nuclei in liquids. The relationship between the radius of nuclei and the cavitation was investigated by Or et al. [7].

In cavitation researches, the issues of gas-liquid two-phase flow have caught many attentions. The lattice Boltzmann method (LBM) has emerged as a powerful tool for simulating the behavior of complex multiphase fluid systems [8]. Based on the thermodynamic LBM with a full coupling of temperature, Zhang et al. [9] predicted the liquid-vapor boiling process, including liquid-vapor formation and coalescence. Yu et al. [10] carried out LBM simulations to obtain the bubble shape, bubble size, and formation mechanism in different mixer geometries of micro-channel sat different flow rates. A two-dimensional (2D) 9-velocity LBM using a single relaxation time (SRT) was developed for immiscible binary fluids with variable viscosities and density ratio [11]. Based on LBM, gas-liquid two-phase flows in a micro porous structure was numerically investigated for various capillary numbers at low Reynolds numbers [12]. Cristea et al. [13] studied the phase separation of a 2D van der Waals fluid subject to a gravitational force based on LBM combined a finite difference scheme. Diop et al. [14] employed 2D LBM to study multiple gas bubbles growing under buoyancy and electromagnetic forces in a quiescent incompressible fluid.

In recent years, many researchers have focused on Shan-Chen multiphase LBM (hereafter referred to as Shan-Chen model) [15, 16] to solve gas-liquid two-phase flow problems. Shan-Chen model was widely applied as a suitable tool for the immiscible two-phase flow in porous media [17]. Huang et al. [18] proposed a method to approximate the adhesion parameters in Shan-Chen model, which can provide the desired fluid-solid contact angle. Kimet al. [19] used D2Q9 Shan-Chen model to capture cavitation formation and its behavior. Qiu et al. [20] presented a multi-component and multiphase LBM combined with a passive-scalar approach and investigated natural convection in the case of a bubble with two different immiscible fluids in a 2D square cavity.

The non-local interactions between fluid particles at neighboring lattice sites were fulfilled by adding an additional forcing term to the velocity particle distributions in Shan-Chen model [15, 16]. Phase separation occurs by choosing an appropriate EOS (equation of state), which is controlled by the interaction potentials. A 2D cavitation "bubble" growth under shear flows was investigated using Shan-Chen model [21], and numerical

https://doi.org/10.4208/cicp.OA-2016-0112 Published online by Cambridge University Press

results show that the cavitation bubble deformation is coincident with Rayleigh-Plesset and other bubble dynamic models, and the bubble growth decreases slightly with the flow shear rate. Zhang et al. [22] incorporated Shan-Chen model with van der Waals EOS to investigate 3D heterogeneous cavitation in liquid successfully. However, the liquid-vapor density ratio is quite smaller than the real value by using van der Waals EOS. Yuan et al. [23] introduced and discussed the incorporation of five various EOS into the single-component multiphase LBM. The spurious current, density ratio, and temperature range were analyzed for different EOSs. The exact difference method (EDM) and the C-S (Carnahan-Starling) EOS coupled with the Shan-Chen model was validated as a suitable tool for simulating high liquid-vapor density ratio in multiphase flows [1]. Yang et al. [24] used the coupling C-S EOS and EDM based on modified Shan-Chen model to investigate the bubble form evolution, collapse time and dynamic character under 2D press fields.

Among cavitation works mentioned-above, most of the previous studies are based on 2D cavitation bubbles, there are few detailed researches on 3D cavitation bubbles. In present paper, 3D cavitation simulations were carried out by using D3Q19 model and Shan-Chen model coupled with C-S EOS. The phase separation processes were simulated in several different temperatures. The relationship between temperature and vapor-liquid density ratio was studied. Surface tension was computed and Laplace law was validated. During 3D cavitation bubble calculations, a pair of pressure boundary conditions and two pairs of periodic boundary conditions were adopted here. The pressure boundary condition on D3Q19 model was derived in detail. The influences of bubble critical radius, pressure difference inside and outside the bubble and temperature on cavitation bubble were analyzed in detail. And the whole processes of cavitation bubble formation, development and collapse were investigated for the first time. This research has important significance for solving large density radio liquid-vapor two-phase flows and provide guidance for numerical study on cavitation bubble in practical applications.

2 Mathematical model

2.1 Lattice Boltzmann model

The D3Q19 LBM (Fig. 1) employed here has discrete velocity vector defined as

$$\boldsymbol{E}=c\begin{bmatrix} 0 & 1 & -1 & 0 & 0 & 0 & 0 & 1 & -1 & 1 & -1 & 0 & 0 & 0 & 0 & 1 & -1 & 1 & -1 \\ 0 & 0 & 0 & 1 & -1 & 0 & 0 & 1 & -1 & -1 & 1 & 1 & -1 & 1 & -1 & 0 & 0 & 0 & 0 \\ 0 & 0 & 0 & 0 & 0 & 1 & -1 & 0 & 0 & 0 & 0 & 1 & -1 & -1 & 1 & 1 & -1 & -1 & 1 \end{bmatrix}, \tag{2.1}$$

where $c=\Delta x/\Delta t$ is the lattice speed, Δt is time step and Δx donates the lattice spacing. The LB equation (LBE) is presented as

$$f_i(\mathbf{x}+\mathbf{e}_i\Delta t,t+\Delta t)=f_i(\mathbf{x},t)-\frac{1}{\tau}[f_i(\mathbf{x},t)-f_i^{eq}(\mathbf{x},t)]. \tag{2.2}$$

https://doi.org/10.4208/cicp.OA-2016-0112 Published online by Cambridge University Press

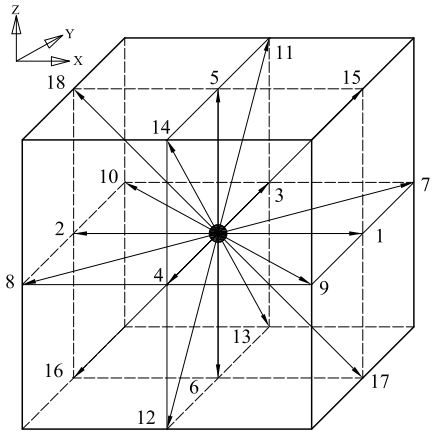


Figure 1: D3Q19 model.

Lattice Bhatnagar-Gross-Krook (LBGK) collision scheme describing the evolution of particle distribution function (PDF) in space and time is applied. τ is the single relaxation time. $f_i(\mathbf{x},t)$ represents PDF along the i^{th} direction at position $\mathbf{x}$ and time t, $f_i^{eq}(\mathbf{x},t)$ is its corresponding local equilibrium distribution function, which reads

$$f_i^{eq}(\mathbf{x},t)=w_i\rho(\mathbf{x})\left[1+\frac{3\mathbf{e}_i\cdot\mathbf{u}}{c^2}+\frac{9(\mathbf{e}_i\cdot\mathbf{u})^2}{2c^4}-\frac{3\mathbf{u}^2}{2c^2}\right], \tag{2.3}$$

where w_i refers to weighting factors, which are $1/3$ for the rest particles $i=0$, $1/18$ for $i=1,2,\cdots,6$ and $1/36$ for $i=7,8,\cdots,18$ in D3Q19 model.

The macroscopic equations can be obtained by using Taylor and Chapman-Enskog expansions to lattice Boltzmann equation (LBE)

$$\frac{\partial\rho}{\partial t}+\nabla\cdot(\rho\mathbf{u})=0, \tag{2.4}$$

$$\frac{\partial(\rho\mathbf{u})}{\partial t}+\nabla\cdot(\rho\mathbf{u}\mathbf{u})=-\nabla p+\nabla\cdot\left[\rho\nu(\nabla\mathbf{u})+(\nabla\mathbf{u})^T\right]. \tag{2.5}$$

The macroscopic density ρ and the macroscopic velocity $\mathbf{u}$ are calculated by

$$\rho=\sum_{i=0}^{18}f_i, \tag{2.6}$$

$$\mathbf{u}=\frac{1}{\rho}\sum_{i=0}^{18}\mathbf{e}_i f_i. \tag{2.7}$$

2.2 Equations of state in single-component multiphase LBM model

The separation of a fluid system into different phases is caused by interactions (or forces) between fluid particles. According to Shan-Chen model, long-range interaction forces

https://doi.org/10.4208/cicp.OA-2016-0112 Published online by Cambridge University Press

between the particles lead to phase separation for both single and multiple components if they are large enough [1]. The interactive force $\mathbf{F}(\mathbf{x},t)$ between nearest neighbor particles is given by

$$\mathbf{F}(\mathbf{x},t)=-G\psi(\mathbf{x},t)\sum_{i=0}^{18}w_i\psi(\mathbf{x}+\mathbf{e}_i\Delta t,t)\mathbf{e}_i, \tag{2.8}$$

where G is the interaction strength and $\psi(\mathbf{x},t)$ is the interaction potential.

For the LBM EOS proposed by Shan-Chen model [15, 16], the pressure function is of the form with van der Waals (vdW) EOS

$$P=\rho RT+\frac{GRT}{2}[\psi(\rho)]^2. \tag{2.9}$$

In addition, some other different EOSs have been incorporated with LB Shan-Chen model for multiphase flows. These EOSs include Redlich-Kwong (R-K) EOS, Redlich-Kwong Soave (RKS) EOS, Peng-Robinson (P-R) EOS and Carnahan-Starling (C-S) EOS. Their expressions are given as follow.

$$\text{R-K EOS:}\qquad p=\frac{\rho RT}{1-b\rho}-\frac{a\rho^2}{\sqrt{T}(1+b\rho)}, \tag{2.10}$$

$$\text{RKS EOS:}\qquad p=\frac{\rho RT}{1-b\rho}-\frac{a\alpha(T)\rho^2}{1+b\rho}, \tag{2.11}$$

$$\text{P-R EOS:}\qquad p=\frac{\rho RT}{1-b\rho}-\frac{a\alpha(T)\rho^2}{1+2b\rho-b^2\rho^2}, \tag{2.12}$$

$$\text{C-S EOS:}\qquad p=\rho RT\frac{1+b\rho/4+(b\rho/4)^2-(b\rho/4)^3}{(1-b\rho/4)}-a\rho^2, \tag{2.13}$$

where a represents the attraction parameter and b stands for the repulsion parameter. Numerical behaviors were compared with each other for different EOS incorporated into the LBM in relevant literatures. The C-S EOS showed better performance in simulations, such as, larger density ratio, wider temperature range, and much smaller spurious currents. It is worth mentioning that the algorithm has higher stability by using C-S EOS, even if the density ratio reaches 10^3 [23].

Considering the superiorities of C-S EOS, it is incorporated into LBM in the present paper to simulate 3D phase separation and cavitation. The relationship between the parameters a, b and the critical properties in C-S EOS are known as [23]

$$a=0.4963R^2T_c^2/p_c,\quad b=0.18727RT_c/p_c. \tag{2.14}$$

Here, $a=1$, $b=4$, $R=1$ are set in our simulations. The interaction potential $\psi(\mathbf{x},t)$ from C-S EOS can be obtained by

$$\psi(\rho)=\sqrt{\frac{6(p-\rho c_s^2)}{G}}. \tag{2.15}$$

https://doi.org/10.4208/cicp.OA-2016-0112 Published online by Cambridge University Press

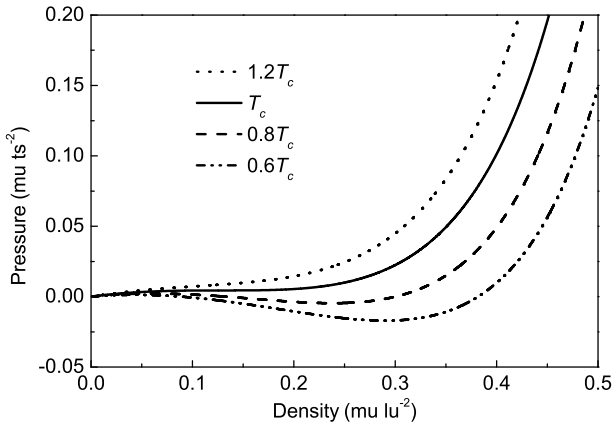


Figure 2: Density and pressure relationship in C-S EOS.

At a high temperature, inter-molecule attraction is weak and the random motion of molecules is dominant [25]. Therefore, a fluid cannot separate into two phases. Once the temperature is reduced below a critical value

$$T_{\rm c}=0.3773a/bR, \tag{2.16}$$

the molecular attraction becomes strong enough to induce phase segregation [20]. The relationship between temperature, pressure and density for a given substance is described by the EOS, and this relationship in C-S EOS is shown in Fig. 2. When $T<T_{\rm c}$, as the pressure decreases, the fluid density reduced following the EOS in the high-pressure region. When the pressure reaches a very negative value, it stops dropping at this point, the occurrence of this point on the C-S EOS is known as the spinodal and corresponds to cavitation. Then the density drops without any additional pressure reduction.

The typical LBE with external force term has the following form [3]

$$f_i(\mathbf{x}+\mathbf{e_i}\Delta t,t+\Delta t)=f_i(\mathbf{x},t)-\frac{1}{\tau}[f_i(\mathbf{x},t)-f_i^{eq}(\mathbf{x},t)]+\Delta f_i. \tag{2.17}$$

where the additional term Δf_i is calculated with $\Delta\mathbf{u}=\mathbf{F}\Delta t/\rho$

$$\Delta f_i=f_i^{eq}(\rho,\mathbf{u}+\Delta\mathbf{u})-f_i^{eq}(\rho,\mathbf{u}). \tag{2.18}$$

In addition, the lattice unit is adopted for all data in present paper. All the lu, mu, ts and Tu stand for LBM length, mass, time and temperature units, respectively. The conversion [26] from lattice units system to physical unit system is made through a length scale factor S_l and a velocity scale factor S_u

$$S_l=l^{ps}\Big/l^{ls}, \tag{2.19}$$

$$S_u=c_s^{ps}\Big/c_s^{ls}, \tag{2.20}$$

https://doi.org/10.4208/cicp.OA-2016-0112 Published online by Cambridge University Press

where the parameters l, c_s represent the length and the sound speed, and the superscript "ls" and "ps" denote these parameters are in lattice unit system or in physical unit system. The Reynolds number Re as a dimensionless parameter are the same in two unit systems. And then, the following formula can be derived

$$S_l S_u = \frac{v^{ps}}{v^{ls}} \Rightarrow S_l = \frac{c_s^{ls} v^{ps}}{c_s^{ps} v^{ls}}, \tag{2.21}$$

where v^{ps} and v^{ls} are the viscosity. A time scale factor S_t can be obtained by using the length scale factor S_l and the velocity scale factor S_u

$$S_t = \frac{t^{ps}}{t^{ls}} = \frac{S_l}{S_u} = \left(\frac{c_s^{ls}}{c_s^{ps}}\right)^2 \frac{v^{ps}}{v^{ls}}. \tag{2.22}$$

The pressure p, the temperature T and the density rho also can be converted between the lattice unit system and the physical unit system by following equations [27]

$$\begin{aligned} p^{ls}/p_c^{ls} &= p^{ps}/p_c^{ps}, \\ T^{ls}/T_c^{ls} &= T^{ps}/T_c^{ps}, \\ \rho^{ls}/\rho_c^{ls} &= \rho^{ps}/\rho_c^{ps}, \end{aligned} \tag{2.23}$$

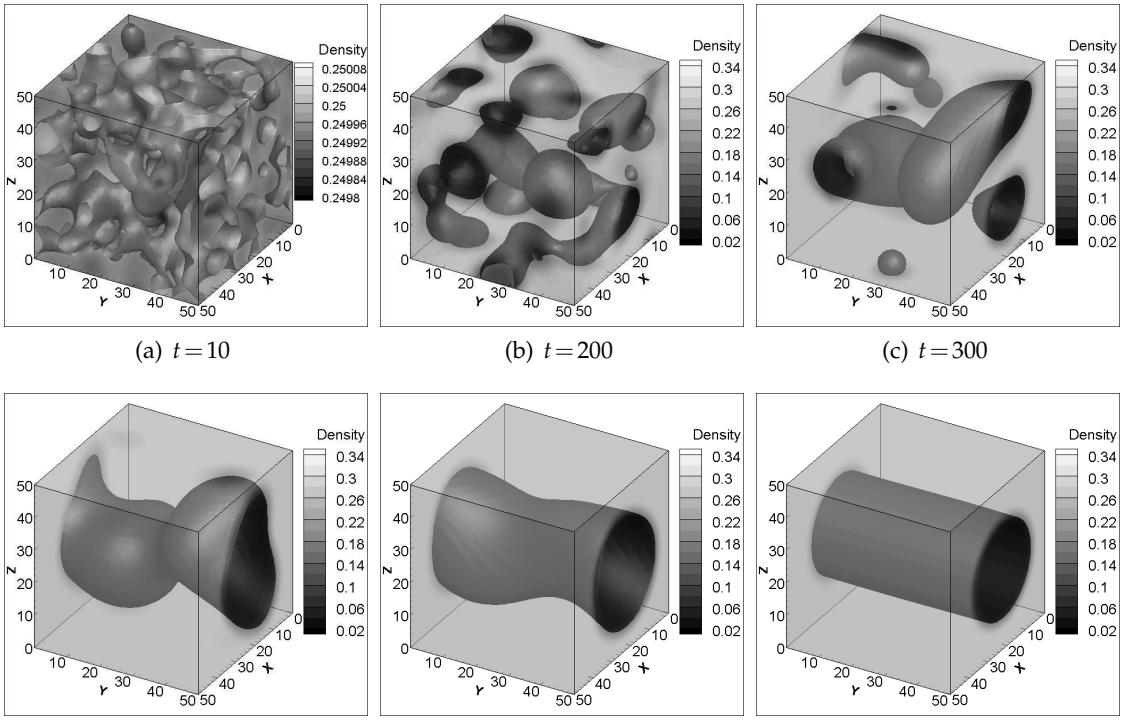
where p_c^{ls}, T_c^{ls} and ρ_c^{ls} are calculated by Eqs. (2.13), (2.14), (2.16). Based on the above-mentioned, there are conversions of size, time and properties between lattice unit system and physical unit system by Eqs. (2.21)-(2.23).

3 Simulation results and discussions

3.1 Phase separation

Aiming at the significant advantage in using C-S EOS and LBM combination model for larger density ratio, the range and the effect of temperature were studied and discussed here. According to the analysis above, it is possible for liquid phase and vapor phase to co-exist when $T < T_c$. To obtain the densities of liquid phase and vapor phase in equilibrium state, 3D phase separation simulations were carried out by using a computational cubic domain of $50\times50\times50$ with periodic boundary conditions, and several different cases with the temperatures ranging from $T = 0.5T_c$ to $T = 0.95T_c$ were considered. The initial values of density in computational domain are taken as $\rho_0 + (0.001 - N_{ran}/10^4)$, where N_{ran} is a random number between 0 and 20, initial average density $\rho_0 = 0.25$. The initial velocities on all nodes are set to be zero. The numerical evolution of mass density distributions during the phase separation process is shown in Fig. 3. Here the case at temperature $T = 0.7T_c$ is taken as an example. It is evident that the system gradually changes from a single-phase fluid to two phase in Fig. 3. After 1000 time steps, these two-phase

https://doi.org/10.4208/cicp.OA-2016-0112 Published online by Cambridge University Press



(a) $t=10$ (b) $t=200$ (c) $t=300$

(d) $t=400$ (e) $t=500$ (f) $t=1000$

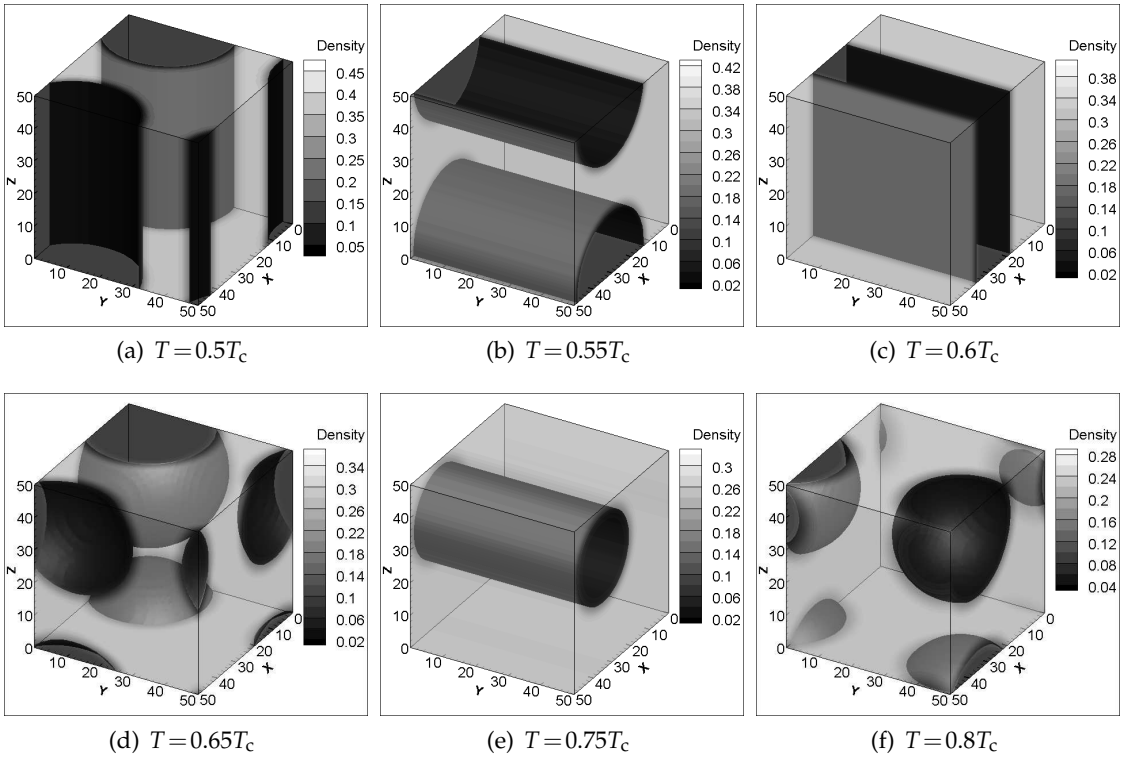
Figure 3: Mass density distributions at $T=0.7T_c$ in 3D phase separation process.

fluid is stable at the equilibrium state, the region occupied by the vapor phase is in the form of cylinder with constant vapor density $\rho_v=0.0047$ and liquid density $\rho_l=0.3541$ outside the cylinder. The corresponding pressure of two phase calculated by the C-S EOS are $p_v=0.0002941$ and $p_l=-0.0008685$.

For different temperature, the mass density distributions in equilibrium state are shown in Fig. 4. The vapor-phase region may form randomly three different shapes including sphere, cylinder and cube at equilibrium state. One of them may appear at any position of the computational domain eventually. The comparisons between the numerical obtained here and those of 2D phase separation given in relevant literatures [15, 28] show that both results are qualitatively similar to some degrees. A circle or a rectangle vapor region are obtained in equilibrium state by 2D simulation in relevant literatures. By contrast, 3D simulation provided in present paper can capture more stereoscopic, direct and real results which provide more information.

The simulated densities in vapor phase and liquid phase at different temperature are listed in Table 1. The density ratios over 2×10^4 were captured successfully, and such high liquid-vapor expands the application scope of two-phase flows in existing cavitation studies. And when the temperature $T=0.593691T_c$, the density ratio is just 10^3. The numerical results, shown in Fig. 5, reveal that the liquid-vapor density ratio at lower

https://doi.org/10.4208/cicp.OA-2016-0112 Published online by Cambridge University Press



(a) $T=0.5T_c$ (b) $T=0.55T_c$ (c) $T=0.6T_c$

(d) $T=0.65T_c$ (e) $T=0.75T_c$ (f) $T=0.8T_c$

Figure 4: Mass density distributions at equilibrium state for different temperature.

Table 1: Density at equilibrium state for different temperature.

T/T_c	ρ_v	ρ_v	ρ_l/ρ_v
0.5	0.000022	0.4556	20709.73
0.55	0.000090	0.4299	4776.79
0.6	0.000503	0.3997	794.72
0.65	0.001642	0.3776	229.94
0.7	0.004706	0.3541	75.25
0.75	0.009484	0.3287	34.66
0.8	0.015760	0.3004	19.06
0.85	0.027001	0.2748	10.18
0.9	0.043454	0.2470	5.68
0.95	0.071397	0.2149	3.01

temperature is bigger compared with that at higher temperature. These results are in good agreement with C-S EOS and larger density ratio can be obtained by decreasing temperature. Nevertheless, temperature cannot be decreased infinitely because of the

https://doi.org/10.4208/cicp.OA-2016-0112 Published online by Cambridge University Press

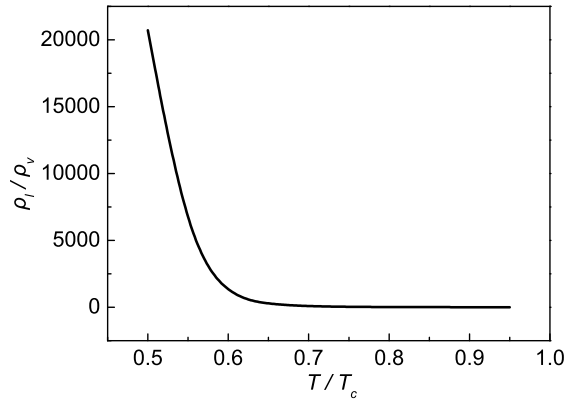


Figure 5: Relationship between liquid-vapor density ratio and temperature.

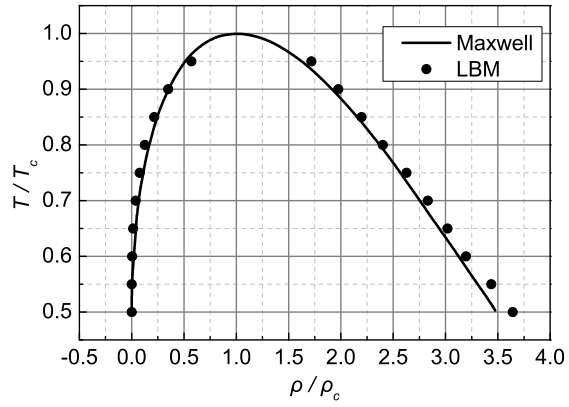


Figure 6: Coexistence curves (Maxwell and LBM).

numerical stability. When $T \leq 0.55T_c$, the density ratio increases rapidly with temperature decrease, and the algorithm becomes unstable.

In order to check the feasibility and the accuracy of the proposed algorithm, the numerical values of density are compared with Maxwell equal-area rule, and the binodal curve is plotted in Fig. 6. The predicted results qualitatively match with Maxwell equal-area rule well. But the liquid density exist a little deviation with the temperature decreasing. This very small error for EOS are tolerable until $T/T_c \leq 0.55$, in which algorithm may become unstable. It is due to the spurious currents exist in numerical results of two-phase flow simulations based on Shan-Chen model. Large spurious currents will make the simulation unstable. The research by Yuan et al. [23] showed that the maximum magnitude of spurious current increases as the temperature decrease, and increases significantly when the temperature below a certain value. For considering calculation accuracy, conditions of $T/T_c > 0.55$ are used for cavitation simulation in the following research.

https://doi.org/10.4208/cicp.OA-2016-0112 Published online by Cambridge University Press

3.2 Cavitation simulations

3.2.1 Energy barrier theory

This study mainly focuses on the heterogeneous cavitation, which occurs when an original tiny bubble of liquid vapor or air acts as a cavitation seed in flow fields and a right pressure-tension relationship can cause the bubble expanding as the surrounding liquid phase change into the vapor phase [6]. Or et al. [7] presented the energy barrier theory to expound this relationship and the total energy cost for cavitation: the sum of the interfacial energy needed to form a new bubble and the work of negative pressure over the bubble volume compose the total energy cost of creating a bubble

$$\Delta E = 4\pi r^2\sigma + \frac{4}{3}\pi r^3\Delta p, \tag{3.1}$$

where σ is the liquid-vapor surface tension, r is bubble radius and $\Delta p = p_{out} - p_{in}$ is the negative pressure relative to the vapor pressure. p_{in} stands for the vapor pressure inside the bubble and p_{out} donates the liquid pressure outside the bubble. When the bubble radius is at the critical value $r^* = -2\sigma/\Delta p$, the maximum value $\Delta E_{\max} = 16\pi\sigma^2/3\Delta p$ for the energy barrier is cost. When the vapor bubble radius is larger than r^*, it grows gradually, namely, the cavitation happens. Otherwise, the bubble with a smaller radius that cannot overcome the energy barrier; it will condense and eventually disappear.

3.2.2 Surface tension

Series of spherical bubbles with various radii were simulated to estimate the surface tension. In each case, a static bubble is placed in the center of a $100\times100\times100$ calculation domain with liquid phase outside the bubble at initial and periodic boundary conditions are used. The maximum relative differences of the magnitude of the pressures at time t and time $t-1$ are on the order of 10^{-6}, which means the steady state is reached. Then the vapor and liquid pressure keep invariable. For example, when the temperature $T=0.7T_c$ and the bubble radius $r=30$, the pressure distribution is shown in Fig. 7. The bubble radii and their corresponding pressure difference Δp inside and outside the bubble are plotted in Fig. 8. There is a linear relationship between pressure difference Δp and the reciprocals of bubble radius $1/r$, and the results are in agreement with Laplace law

$$\Delta p = \sigma/r. \tag{3.2}$$

The slope of a plot of $1/r$ versus Δp is the surface tension σ. For a given temperature condition, the surface tension is constant. The temperature $T=0.65T_c$ and $T=0.7T_c$, at which the simulations have high stability and the large density ratio could be achieved, were chosen as representative for the following cavitation simulations. For the parameters given above, surface tensions of $\sigma=0.0283$ and $\sigma=0.0246$ at temperature $T=0.65T_c$ and $T=0.7T_c$ were obtained respectively. From this, at a specified temperature and pressure difference condition, a certain critical radius of cavitation occurrence is determined.

https://doi.org/10.4208/cicp.OA-2016-0112 Published online by Cambridge University Press

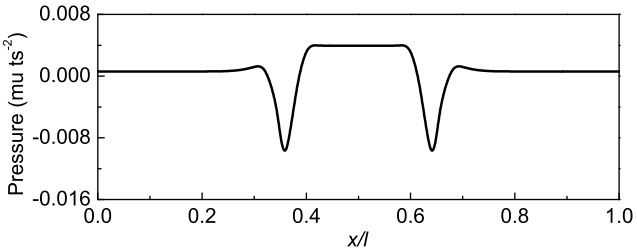


Figure 7: Pressure distribution ($T=0.7T_c$, $r=30$).

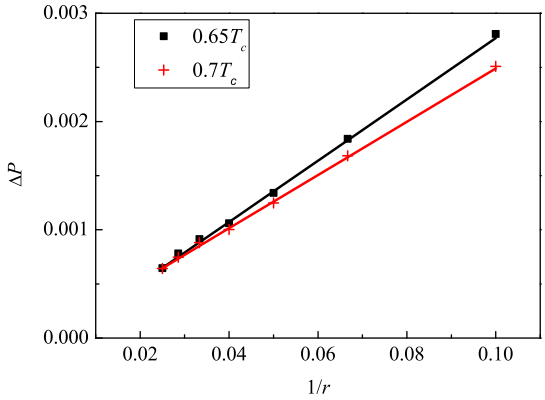


Figure 8: Validation of Laplace law.

3.2.3 Boundary conditions

To illustrate the cavitation simulations of LBM coupled with C-S EOS, the evolution of the static spherical vapor bubble is presented for a 3D single-component two-phase flow system. In the computational domain, the constant pressure boundary conditions are applied on a pair of surface boundary on y-z plane as shown in Fig. 9. The periodic boundary conditions are imposed on the rest of the boundaries. These boundary conditions can make an environment for promoting fluid flow and the occurrence of cavitation. For details, pressure boundary condition setting is discussed here.

The pressure boundary condition in D3Q19 model is used based on Zou-He boundary condition [29]. Suppose a flow boundary (plane 1 shown in Fig. 4 is taken as an example) perpendicular to the x-direction, and the density ρ is specified on the plane 1. The velocities u_y and u_z are also specified as zero here. The PDFs $f_i(e_{ix}\leq 0)$ shown in Fig. 1 are known after streaming. Only the velocities u_x and PDFs $f_i(e_{ix}>0)$ need to be worked out. According to Eq. (2.7), the expression of x-momentum gives

$$\rho u_x=\sum f_i(e_{ix}>0)-\sum f_i(e_{ix}<0). \tag{3.3}$$

https://doi.org/10.4208/cicp.OA-2016-0112 Published online by Cambridge University Press

Consistency of the Eqs. (2.6), (3.3), velocities u_x can be determined by ρ and $f_i(e_{ix}\leq 0)$

$$u_x = 1-\frac{1}{\rho}[2\sum f_i(e_{ix}<0)+\sum f_i(e_{ix}=0)], \quad \alpha = x,y,z. \tag{3.4}$$

To obtain other unknown after-streaming PDFs $f_i(e_{ix}>0)$ including f_1, f_7, f_9, f_{15}, f_{18}, bounce-back rule is used for the non-equilibrium term of the particle distribution normal to the boundary

$$f_i - f_i^{eq} = f_{\bar{i}} - f_{\bar{i}}^{eq}. \tag{3.5}$$

The distribution function f_1 along the x-direction can be calculated

$$f_1 = f_2 + \frac{1}{3}\rho u_x. \tag{3.6}$$

In order to get the correct y-, z- momenta, PDFs $f_i(f_7, f_9, f_{15}, f_{18})$ are modified to $f_i + \frac{1}{2}e_{iy}\delta_y + \frac{1}{2}e_{iz}\delta_z$. Substituting the modified f_i into Eq. (3.5), after-streaming PDFs f_7, f_9, f_{15}, f_{18} are obtained

$$\begin{aligned}
f_7 &= f_8 + \frac{1}{6}\rho u_x - \frac{1}{2}(f_3 - f_4 + f_{11} - f_{12} + f_{13} - f_{14}),\\
f_9 &= f_{10} + \frac{1}{6}\rho u_x - \frac{1}{2}(f_4 - f_3 - f_{11} + f_{12} - f_{13} + f_{14}),\\
f_{15} &= f_{16} + \frac{1}{6}\rho u_x - \frac{1}{2}(f_5 - f_6 + f_{11} - f_{12} - f_{13} + f_{14}),\\
f_{17} &= f_{18} + \frac{1}{6}\rho u_x - \frac{1}{2}(f_6 - f_5 - f_{11} + f_{12} + f_{13} - f_{14}).
\end{aligned} \tag{3.7}$$

3.2.4 Numerical validation

In order to verify the feasibility of the model used here, cavitation bubble simulations were carried out with different radii at the same temperature $T=0.7T_c$ and the same pressure difference $\Delta p = -0.004$. At this situation, the critical bubble radius was calculated as $r^* = 12.3$. The vapor bubbles were inserted with two initial radii $r_1 = 12 < r^* < r_2 = 13$ in two cases, respectively. The grid independent analysis was carried out with three various grid resolutions to make sure the accuracy of the numerical results. Given an initial radius $r_1 = 12$, the variations of bubble radius versus time are given in Fig. 10 with the $80\times80\times80$ lattice, the $100\times100\times100$ lattice, the $120\times120\times120$ lattice and the $160\times160\times160$ lattice. There is a minor deviation of numerical results in the $80\times80\times80$ lattice from those in other three finer meshes, and the numerical results are much the same by using the $100\times100\times100$ lattice, the $120\times120\times120$ lattice and the $160\times160\times160$ lattice. A computational domain of $100\times100\times100$ lattice is used here to simulate the cavitation bubble eventually.

The numerical results of cavitation bubble evolution are shown in Fig. 11. The occurrence of vapor bubble cavitation and condensation were numerical simulated, respectively. When the value of the bubble radius is above the critical value, the bubble expands

https://doi.org/10.4208/cicp.OA-2016-0112 Published online by Cambridge University Press

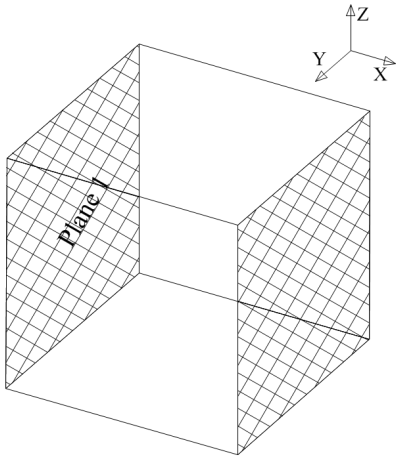


Figure 9: Boundary diagram.

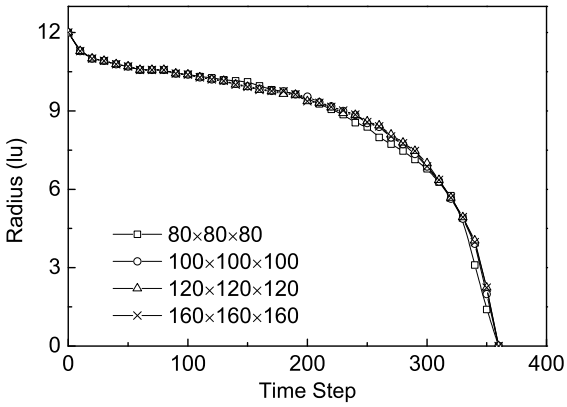
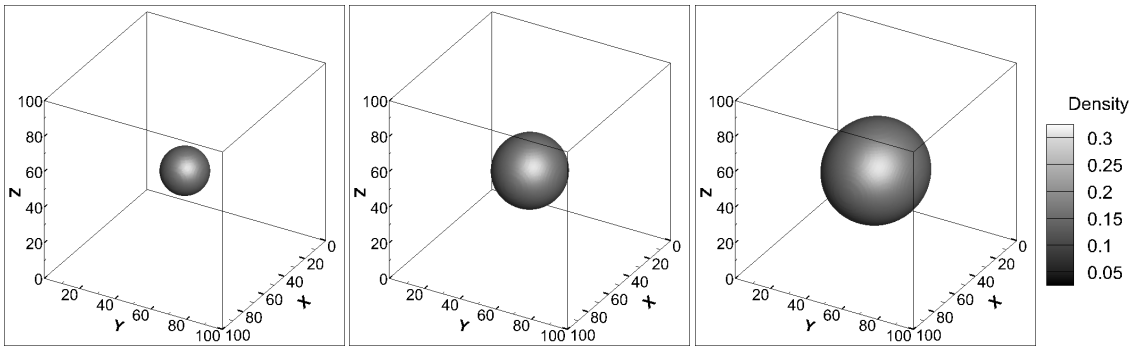
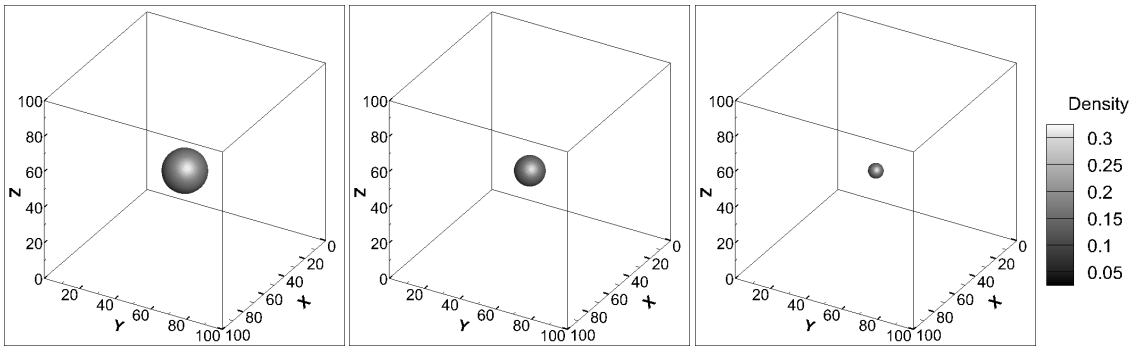


Figure 10: Grid independent analyses.



$t=10$ $t=600$ $t=800$

(a) Initial bubble radius $r=13$



$t=10$ $t=280$ $t=340$

(b) Initial bubble radius $r=12$

Figure 11: Bubble evolution at $T=0.7T_c$, $\Delta p=-0.004$.

https://doi.org/10.4208/cicp.OA-2016-0112 Published online by Cambridge University Press

as the surrounding liquid phase changes into the vapor phase as shown in Fig. 11(a). The cavitation occurs and the volume of the bubble increases continually. On the contrary, when a bubble with the initial radius ($r_1=12$) is smaller than the critical radius, the bubble becomes smaller obviously after 280 time steps and almost disappears after 340 time steps.

The above simulation results are in good agreement with energy barrier theory. The effectiveness and reliability of Shan-Chen multiphase LBM model coupled with C-S EOS presented in this paper are verified in cavitation bubble simulations. Compared with other 2D studies [1,21,23], 3D cavitation simulation researches here are more consistent with actual rules of cavitation occurrence and condensation.

3.2.5 Cavitation Bubble Results Analyses

The influence of pressure difference, temperature and existed bubble nuclei radius on cavitation in flow fields [21] is analyzed here. There are four combination cases, $T=0.65T_c$, $T=0.7T_c$, $\Delta p=-0.004$ and $\Delta p=-0.005$ are chosen here and the corresponding numerical results of critical bubble radii are given in Table 2. As the temperature increases by $0.05T_c$ Tu, the corresponding critical radius decreases by about 2 lu. Moreover, as the pressure difference reduces by 0.001 mu ts^{-2}, the critical radius increases by about 3 lu. In other words, at lower temperature and lower pressure difference condition, critical radius is larger and thus the bubble cavitation is harder to occur.

Table 2: Critical bubble in different pressure difference and different temperature.

	$T=0.65T_c$	$T=0.7T_c$
$\Delta p=-0.004$	$r^*=14.15$	$r^*=12.3$
$\Delta p=-0.004$	$r^*=11.32$	$r^*=9.84$

Aiming at four conditions listed above, the initial bubble radius $r_{initial}$ is taken as a value of integer portion of r^*, and the evolution of the bubble radius is shown in Fig. 12(a) for the processes of vapor bubble collapse. Here, the liquid and the vapor interface is defined as $\rho_{\text{inter}}=(\rho_l+\rho_v)/2$, and the corresponding bubble radius r is specified as the distance between interface and spherical bubble center as shown in Fig. 13. The variation regularities of bubble radii in collapse processes are highly similar at different temperature and different pressure difference. According to the energy barrier theory, the surface tension and the pressure difference both do work on the vapor bubble in its evolution process. When the bubble radius r is smaller than the critical value r^*, the work of the surface tension part $E_s=4\pi r^2\sigma$ has dominant contribution, and the bubble is forced to shrink. The derivative of the energy E_s to the bubble size is $\dot{E}_s=8\pi\sigma r$, and the derivative of the energy E_p (the work of pressure difference part on the vapor bubble $E_p=\frac{4}{3}\pi r^3\Delta p$) to the bubble size is $\dot{E}_p=4\pi\Delta p r^2$.The decrease tendency of the energy E_s is slower than that of the energy E_p, and the energy E_s plays an increasingly important part in the evolution of bubble condensation. Therefore, it can be seen that from Fig. 12(a), the vapor

https://doi.org/10.4208/cicp.OA-2016-0112 Published online by Cambridge University Press

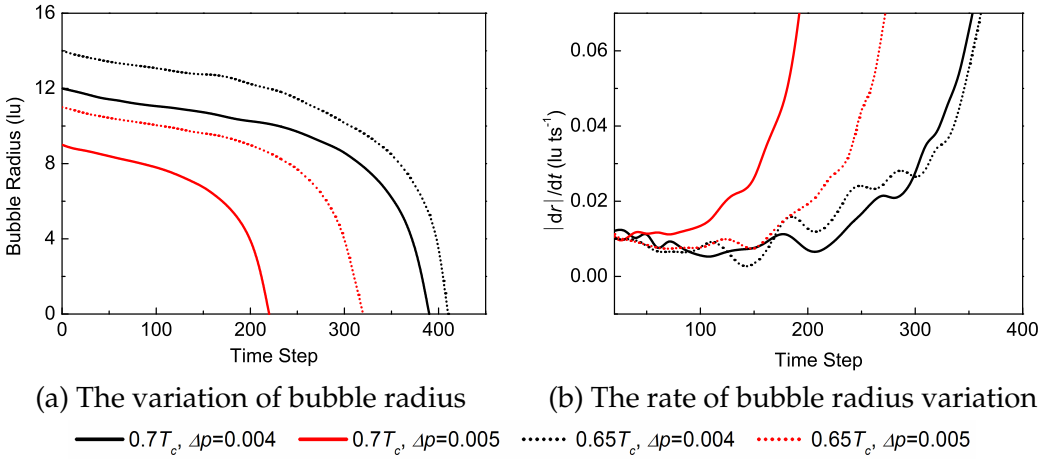


Figure 12: Bubble variation in the process of bubble collapse.

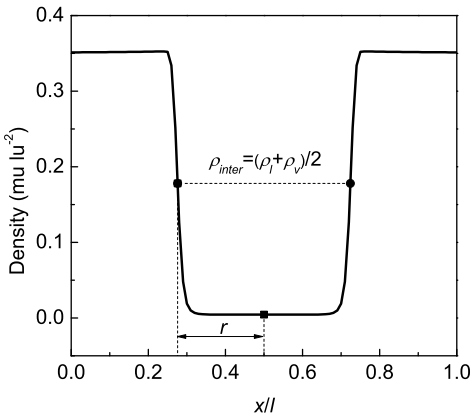


Figure 13: Liquid, vapor and interface density of cavitation bubble.

bubbles shrink slowly at the beginning and the shrinking speeds of the bubbles accelerate with the bubbles' evolution time. At last, the bubbles have collapsed rapidly and then disappear entirely. The variation ratio of bubble radius as another indicator is also presented in Fig. 12(b) for more details. The simulation results show that the time required for a vapor bubble collapse depends on initial bubble radius which is related to critical radius. It is clear that a smaller bubble with radius less than its critical value is easier to collapse at any given temperature and pressure difference.

The integer portion of r^* plus 1 is taken as the initial radius $r_{initial}$, the evolution of bubble cavitation were numerically investigated at the four different cases listed in Table 2. When a bubble radius is just above the critical radius, the bubble could grow without limit while displacing an equal volume of liquid due to the decrease in energy cost with the increase in bubble radius. As shown in Fig. 14(a), cavitation occurs and the bubble

https://doi.org/10.4208/cicp.OA-2016-0112 Published online by Cambridge University Press

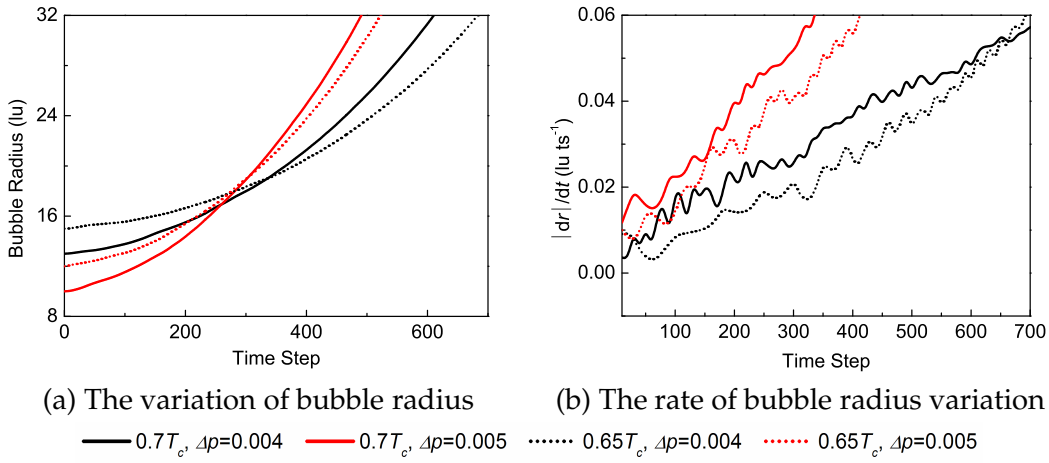


Figure 14: Bubble variation in the process of bubble cavitation.

grows at all given conditions. At any given temperature, less energy barrier is needed to overcome to form a cavitation bubble at larger pressure difference ($\Delta p=-0.005$), and the corresponding bubble critical radius is smaller, so the cavitation occurs more easily and the cavitation bubble grows faster. In the same condition of pressure difference, higher the temperature is, lower the surface tension is, and the corresponding critical bubble is smaller, which means the bubble cavitation occur more easily. At the same time, the work of the surface tension is less and increases slower than the work of the pressure difference. So, at any given pressure difference, the higher the temperature is, the faster the bubble size increases.

The influence of initial existing bubble radius on bubble cavitation was studied. As shown in Fig. 15, the cases of two different pressure differences $\Delta p=-0.004$ and $\Delta p=-0.005$ at temperature $T=0.7T_c$ are analyzed and chosen as the examples. It is evident that, the larger the initial bubble radius is than the critical one, the easier the cavitation is to happen and the faster the cavitation bubble increases in both two pressure difference conditions.

To observe the continuous processes of occurrence, development and collapse of cavitation, cavitation bubble calculations were carried out under pressure-changing boundary conditions fitting engineering realities. A spherical vapor bubble with an initial radius $r_{initial}=16<r^*$ is placed at the center of the computational domain with temperature $T=0.7T_c$. The vapor bubble is surrounded by the liquid, in which pressure changes from initial high value to a low pressure value. The process of continuous variation of cavitation bubble with time t is illustrated in Fig. 16. After 550 time steps, the pre-placing bubble has already shrunk as a tiny nuclei existing in the liquid, that is, bubble collapse. When the environmental pressure reduces to cavitation pressure, the tiny nuclei bubble can overcome the energy barrier and the cavitation bubble occurs, develops gradually during initial stage, and then starts to grow faster.

https://doi.org/10.4208/cicp.OA-2016-0112 Published online by Cambridge University Press

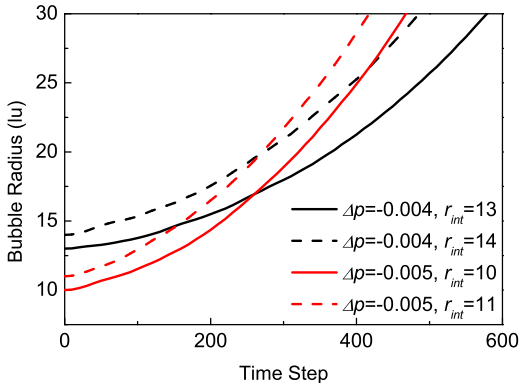


Figure 15: Effect of initial bubble radius on cavitation.

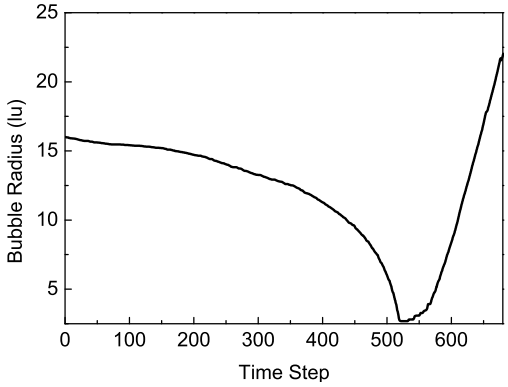


Figure 16: Vapor bubble radius in various pressure condition.

4 Conclusion

In this paper, three-dimensional cavitation bubble by using LBM D3Q19 model was studied based on Shan-Chen model coupled with Carnahan-Starling real-gas EOS. The phase separation processes were simulated at various temperatures from $T=0.5T_c$ to $T=0.95T_c$. The simulated results are quite similar but more stereoscopic, direct and real than the 2D simulations in relevant literatures. High liquid-vapor density ratio over 2×10^4 were captured successfully which expands the application scope of two-phase flows in cavitation studies. The feasibility and the accuracy of the model used in present paper were verified by Maxwell equal-area rule. The relationship between temperature and density ratio, which states that the liquid-vapor density ratio at lower temperature is larger compared with that at higher temperature, is in good agreement with C-S EOS.

Laplace law was validated by simulating series of spherical bubbles with various radii. The bubble radii and their corresponding pressure difference Δp inside and outside the bubble were plotted, and there is a linear relationship between pressure difference

https://doi.org/10.4208/cicp.OA-2016-0112 Published online by Cambridge University Press

Δp and the reciprocals of bubble radius $1/r$. The vapor bubble surface tensions were obtained by the slope of a plot of $1/r$ versus Δp. The surface tensions at $T=0.65T_c$ and $T=0.7T_c$ were calculated as $\sigma=0.0283$ and $\sigma=0.0246$, and the simulations have high stability and the large density ratio could be obtained. The surface tension is smaller at higher temperature than that at lower temperature.

After mesh independence check, cavitation occurrence and condensation were simulated successfully with $100\times100\times100$ lattice. All the numerical simulation results are in good agreement with energy barrier theory, and thus the effectiveness and reliability of Shan-Chen multiphase LBM model coupled with C-S EOS are verified. The results show that, when the bubble radius is larger than the critical value r^*, the cavitation will happen. Otherwise, when the bubble radius is too small to overcome the energy barrier, it will condense.

For cavitation investigations, the influences including pressure difference, temperature and existed bubble nuclei radius were analyzed in detail. Critical radius is larger for lower temperature and lower pressure difference condition, and bubble cavitation is harder to occur. In collapse processes, the variation regularities of bubble radii are similar to each other for different temperature and different pressure difference, and the shrinking-speed of the bubbles accelerates with the bubble-evolution time. The smaller the bubble with its radius less than the critical size is, the easier collapse entirely. It is also found that the bubble cavitation occurs more easily for higher temperature and larger pressure difference, and the expanding velocity of cavitation bubble is faster. In addition, the initial bubble radius is bigger than the critical one, the cavitation is easier to occur and the bubble grows faster. Finally, whole processes of formation, development and collapse of a vapor bubble were captured successfully under various pressure conditions for the first time. All the results and analysis can offer valuable references for further cavitation researches and provide guidance for numerical study on cavitation bubble in practical applications.

Acknowledgments

This work was supported by the National Natural Science Foundation of China (Grant Nos. 51479196, 51179192, 51139007), the Program for New Century Excellent Talents in University (NCET) (Grant No. NETC-10-0784), the National Hi-Tech Research and Development Program of China (”863” Project) (Grant No. 2011AA100505) and the Chinese Universities Scientific Fund (Grant No. 2016QC085).

References

[1] X. Chen, C. Zhong and X. Yuan, Lattice Boltzmann simulation of cavitating bubble growth with large density ratio, Comput, Math. Appl., 61 (2011), 3577-3584.

https://doi.org/10.4208/cicp.OA-2016-0112 Published online by Cambridge University Press

[2] D. Li, M. Grekula and P. Lindell, A modified SST k-ω turbulence model to predict the steady and unsteady sheet cavitation on 2D and 3D hydrofoils, 7th International Symposium on Cavitation (CAV2009), Ann Arbor, Michigan, USA, 2009.
[3] M. Zhong, C. Zhong and C. Bai, A high-order discrete scheme of lattice Boltzmann method for cavitation simulation, Adv. Comput. Sci. Appl., 1 (2012), 73-77.
[4] Y. Zhang and S. Li, A general approach for rectified mass diffusion of gas bubbles in liquids under acoustic excitation, J. Heat. Trans.-T. AMSE, 136 (2014), 158-170.
[5] Y. Zhang, A generalized equation for scattering dross section of spherical gas bubbles oscillating in liquids under acoustic excitation, J. Fluid. Eng.-T. ASME, 135(2013), 091301.
[6] M. C. Sukop and D. Or, Lattice Boltzmann method for homogeneous and heterogeneous cavitation, Phys. Rev. E., 71(2005): 46703.
[7] D. Or and M. Tuller, Cavitation during desaturation of porous media under tension, Water. Resour. Res., 38(2002): 11-19.
[8] M. C. Sukop and D. Or, Lattice Boltzmann method for modeling liquid-vapor interface configurations in porous media, Water. Resour. Res., 40(2004): W01509.
[9] R. Zhang and H. Chen, Lattice Boltzmann method for simulations of liquid-vapor thermal flows, Phys. Rev. E., 67(2003), 066711.
[10] Z. Yu, O. Hemminger and L. Fan, Experiment and lattice Boltzmann simulation of two-phase gas-liquid flows in microchannels, Chem. Eng. Sci. 62(2007): 7172-7183.
[11] T. Reis and T. N. Phillips, Lattice Boltzmann model for simulating immiscible two-phase flows, J. Phys. A.-Math. Theor., 40(2007): 4033-4053.
[12] J. Tomiyasu and T. Inamuro, Numerical simulations of gas-liquid two-phase flows in a micro porous structure, Eur. Phys. J.-SPEC. TOP., 171(2009): 123-127.
[13] A. Cristea, G. Gonnella and A. Lamura et al, A lattice Boltzmann study of phase separation in liquid-vapor systems with gravity, Commun. Comput. Phys., 7(2009), 350-361.
[14] M. Diop, F. Gagnon and L. Min et al, Gas bubbles expansion and physical dependences in aluminum electrolysis cell: from micro- to macroscales using lattice Boltzmann method, ISRN Mater. Sci., 2014(2014), 1-11.
[15] X. Shan and H. Chen, Lattice Boltzmann model for simulating flows with multiple phases and components, Phys. Rev. E., 47(1993), 1815-1819.
[16] X. Shan, and H. Chen, Simulation of nonideal gases and liquid-gas phase-transitions by the lattice Boltzmann-equation, Phys. Rev. E., 49(1994), 2941-2948.
[17] H. Huang, Z. Li and S. Liu et al, Shan-and-Chen-type multiphase lattice Boltzmann study of viscous coupling effects for two-phase flow in porous media, Int. J. Numer. Meth. Eng., 61(2009), 341-354.
[18] H. Huang, D. J. Thorne and M. G. Schaap et al, Proposed approximation for contact angles in Shan-and-Chen-type multicomponent multiphase lattice Boltzmann models, Phys. Rev. E., 76(2007), 66701.
[19] H. Kim and T. Kim, Lattice Boltzmann simulation of cavitation and particle behavior induced by sonication transducer: ECS Transactions, 220th ECS Meeting, 41(2011), 109-113.
[20] R. Qiu, A. Wang and T. Jiang, Lattice Boltzmann method for natural convection with multicomponent and multiphase fluids in a two-dimensional square cavity, Can. J. Chem. Eng., 92(2014), 1121-1129.
[21] X. Chen, Simulation of 2D cavitation bubble growth under shear flow by lattice Boltzmann model, Commun. Comput. Phys., 7(2010), 212-223.
[22] X. Zhang, C. Zhou and S. Islam, et al, Three-dimensional cavitation simulation using lattice Boltzmann method. Chinese, J. Phys., 12(2009), 8406-8414.

https://doi.org/10.4208/cicp.OA-2016-0112 Published online by Cambridge University Press

[23] P. Yuan and L. Schaefer, Equations of state in a lattice Boltzmann Model, Phys. Fluids., 18(2006), 42101.
[24] J. Yang, Z. Shen and X. Zheng et al, Simulation on cavitation bubble collapsing with lattice Boltzmann method, J. Appl. Math. Phys., 3(2015), 947-955.
[25] X. He, S. Chen and R. Zhang, A lattice Boltzmann scheme for incompressible multiphase flow and its application in simulation of Rayleigh-Taylor instability, J. Comput. Phys., 152(1999), 642-663.
[26] Y, He, Y Wang and Q. Li, Lattice Boltzmann method: theory and applications, Science Press, 2009.
[27] J. B. Zeng, L. J. Li and Q. Liao et al, Simulation of phase transition process using lattice Boltzmann method. Chinese, Sci. Bull., 54(2009), 4596-4603.
[28] W. Athasit and C. N. Huang, A novel solution for fluid flow problems based on the lattice Boltzmann method, Mol. Simulat., 13(2014), 1043-1053.
[29] Q. Zou and X. He, On pressure and velocity flow boundary conditions and bounceback for the lattice Boltzmann BGK model, Phys. Fluids., 6(1997), 1591-1598.

https://doi.org/10.4208/cicp.OA-2016-0112 Published online by Cambridge University Press